Low Noise, IR-Blind Organohalide Perovskite Photodiodes for Visible Light Detection and Imaging

Qianqian Lin, Ardalan Armin, Dani M. Lyons, Paul L. Burn, and Paul Meredith**

Silicon photodiodes are currently the workhorse for image sensors used in digital cameras and smartphones. These photodiodes are low noise, broadband, and can deliver high detectivities of $>10^{12}$ J, linear dynamic ranges (LDRs) of >200 dB, and high frequency responses limited only by circuit *RC* characteristic times. However, silicon has a band gap of 1.1 eV leading to an unwanted near-IR photoresponse. In photodiodes, this is a source of optical noise that reduces image quality, and increases architectural complexity and cost to suppress. Other semiconductors with wider optical gaps (and hence less sensitivity in the IR) have been trialed with varying degrees of success including band gap engineered quantum confined nanostructures[1] and organic semiconductors.[2] To replace or rival silicon as the photojunction, any substitute must deliver at least the same figures of merit, but preferably have simpler and cheaper fabrication. For example, quantum dot (QD) visible light photodetectors[3] can achieve high specific detectivities ($>10^{12}$ J) but exhibit modest LDRs (<60 dB), slow temporal (frequency) response (<100 Hz at −3 dB), and large dark currents (>100 μA cm^{-2}) inducing noise and power wastage. Organic photodiodes (OPDs) have also been reported for different spectral ranges,[2,4,5] including broadband visible.[6] These OPDs have metrics approaching that of silicon, and the potential for simple, low-cost processing, but have yet to fully demonstrate their potential. Thus, an ideal substitute for silicon as the active junction in visible light photodiodes is yet to present itself.

Organohalide lead perovskites have recently emerged as a leading next generation thin film solar cell technology.[7,8] Although their basic electrical and optical properties have yet to be fully elucidated, they appear to be polycrystalline direct gap semiconductors with very low exciton binding energies,[9,10] large static dielectric constants (40–70),[9,10] high free carrier mobilities,[11] and a partially tunable energy gap around 1.6 eV.[12,13] These are exactly the properties one could envisage for a wider-gap version of silicon, with the added benefit that perovskite films can be processed by low temperature vacuum evaporation or from solution.[8,13,14]

It might be thought that organohalide perovskite solar cells could in principle be optimized for photodiode operation in the same way as organic solar cells have been.[15] However, this is not the case for a number of reasons: (i) the most common solar cell structure consisting of a mesoporous oxide/perovskite heterojunction[16] cannot be used in a photodiode due to its large effective junction area that dramatically increases parasitic capacitance and dark current (both fatal for photodiode detectivity and temporal response); (ii) the recently introduced alternative planar perovskite solar cell architecture employing either thin organic[17] or inorganic [18] electron/hole transporting layers also possesses a high intrinsic capacitance mainly due to the large dielectric constant of the constituent perovskite;[19] and (iii) solution-processed perovskite junctions deposited on anything other than an appropriate oxide tend, with only a few exceptions, to contain large crystallites in the thin film that lead to roughness and current leakage[20]—in a photodiode this is also disastrous for the dark current. Recently, photoresistors and phototransistors based on organohalide perovskites have been reported.[21–23] However, the properties of these devices are not sufficient for imaging applications or low noise light detection.

In this Communication, we address these issues and demonstrate organohalide perovskite photodiodes (PPDs) with performance metrics equivalent to commercially available silicon photodiodes. Our PPDs are solution processed, completely IR-blind, and have the simplest possible linear homojunction architecture. They employ relatively thick fullerene (n-type organic semiconductor) electron transporting interlayers to manipulate the device electro-optics, from whence we achieve control over junction capacitance, dark current, and frequency response without compromising the LDR.

Figure 1a shows a typical X-ray diffraction (XRD) pattern of a spin-coated polycrystalline film of the organohalide perovskite $CH_3NH_3PbI_3$ on a poly(3,4-ethylenedioxythiophene):poly(styrene sulfonate) (PEDOT:PSS) modified indium tin oxide (ITO) on glass substrate, with the crystal structure shown in the inset. The XRD pattern confirms a high degree of crystallinity and orientation, and is similar to that reported for the best $CH_3NH_3PbI_3$ coevaporated films.[9] The crystallite size (<100 nm) can be seen in the scanning electron microscopy (SEM) image shown in the inset of Figure 1a, and can also be inferred from the diffraction peaks at 14.3° and 28.6° [assigned to the (110) and (220) planes, respectively]. The absorption spectrum of perovskite film is shown in Figure S1 (Supporting Information).

Figure 1b shows the architectures of the four PPD devices, which all have ITO/PEDOT:PSS anodes, an organohalide perovskite homojunction, and lithium flouride (LiF)-modified silver (Ag) cathodes. We categorize the four structures as follows: (i) Type 1 contains a thin solution-processed [6,6]-phenyl-C61-butyric acid methyl ester (PC60BM) layer (≈10 nm); (ii) Type 2 has a thicker PC60BM layer (≈50 nm); (iii) Type 3 contains a thick evaporated C60 layer (≈130 nm); and (iv) Type 4 an optically optimized (see Figure S2, Supporting Information)

Q. Lin, A. Armin, Dr. D. M. Lyons, Prof. P. L. Burn, Prof. P. Meredith
Centre for Organic Photonics & Electronics
School of Chemistry and Molecular Biosciences
and School of Mathematics and Physics
The University of Queensland
Brisbane, Queensland 4072, Australia
E-mail: p.burn2@uq.edu.au; meredith@physics.uq.edu.au

DOI: 10.1002/adma.201405171

ADVANCED MATERIALS
www.advmat.de

www.MaterialsViews.com

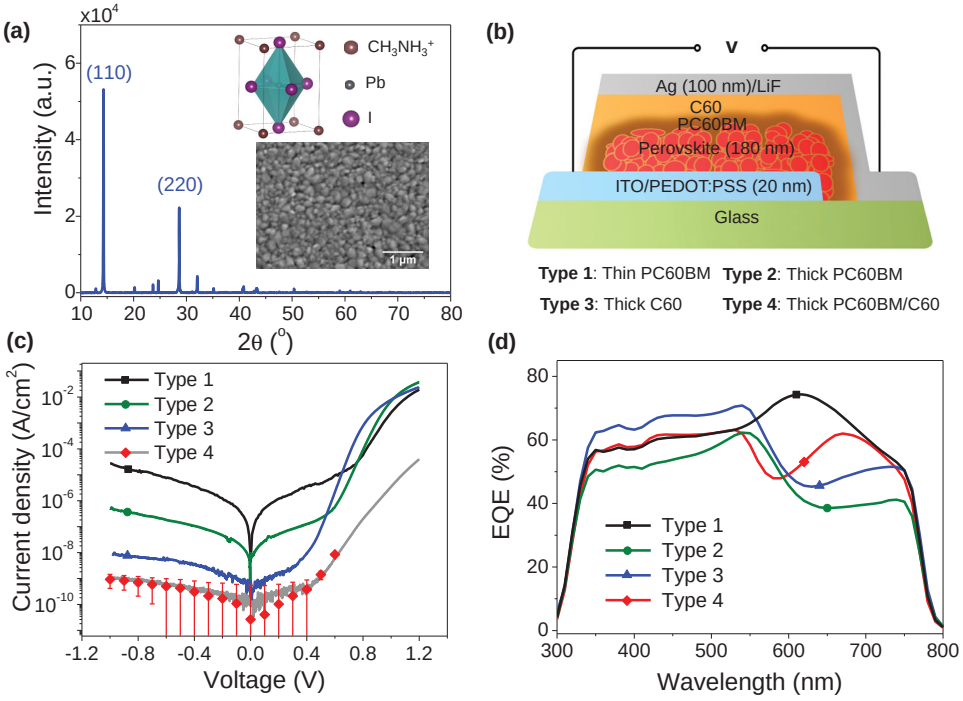

Figure 1. Organohalide perovskite ($CH_3NH_3PbI_3$) photodiodes. a) X-ray diffraction (XRD) pattern of solution processed perovskite films on ITO/PEDOT:PSS with the crystal structure pictured in the inset. The XRD pattern indicates a very strong degree of crystallinity with the crystallite size visible in the scanning electron microscopy (SEM) image shown in the inset. b) Cartoon of the four different PPD structures: Type 1 with thin PC60BM (10 nm) layer, Type 2 with thick PC60BM (50 nm) layer, Type 3 with thick C60 layer, and Type 4 with thick PC60BM (50 nm)/C60 (130 nm) layer. c) Dark current density–voltage (*J*–*V*) characteristics obtained at a scanning rate of 1 mV s^{-1}. Each point shown for the Type 4 devices are an average of the dark current measured over several seconds after each voltage step. d) Typical external quantum efficiency (EQE) spectra (measured at 120 Hz) for each of the four PPD types.

combination of thick PC60BM and C60 layers. The optimization of the layers was done using transfer matrix optical modeling.[24] In all cases, the perovskite homojunction thickness was ≈180 nm as measured by a Dektak profilometer. The fullerene interlayers act to promote electron extraction, and effectively block the back injection of holes to suppress the dark current even under reverse bias. This is due to their poor hole mobility and large ionization potentials.

Figure 1c shows typical dark current density–voltage (*J*–*V*) curves for each of these structures. The thin fullerene interlayers of the Type 1 devices do not completely cover the polycrystalline perovskite junction, and we observe a relatively high reverse bias dark current density of 10^{-5} A cm^{-2} at –0.5 V. The use of thick PC60BM (Type 2) or C60 (Type 3) leads to a significant reduction in the dark current, which is due to better coverage of the perovskite crystallites by the hole blocking fullerene layer. The Type 4 devices exhibited by far the lowest dark currents (5×10^{-10} A cm^{-2} at –0.5 V), which is close to the limit of our measurement system. The electron-transport/hole-blocking layer comprised of individual layers of PC60BM and C60 gave the best overall coverage of the perovskite layer, and hence the most effective reduction of leakage current.

Figure 1d presents typical external quantum efficiency (EQE) spectra (obtained at short circuit condition) for the four types of photodiodes. They all exhibit high EQEs (50%–70%) in the wavelength range 300–800 nm, and hence are suitable for visible-light broadband photodetection. We have previously shown that the EQE response of a $CH_3NH_3PbI_3$ perovskite homojunction solar cell with similar active layer thickness as these OPDs has the following characteristics: i) saturation regime <550 nm where the absorption coefficient is so high that the optical density (OD) is >> 1 (Figure S1, Supporting Information) and therefore, there are minimal cavity effects. The spectral shape in this region does not vary much as a function of the thickness of the perovskite and other layers; and (ii) for wavelengths > 550 nm the OD is =1 (Figure S1, Supporting Information) and the diode operates in the low finesse cavity limit where interference plays a role. The EQE can be optimized by careful optical modeling and controlling the thicknesses of each of the layers.[9,25,26] These basic cavity phenomena are observed in Figure 1d noting that the Type 4 devices were further optimized using transfer matrix analysis to flatten the spectral response (Figure S2, Supporting Information). This structure also delivered an electric field independent EQE confirming a high charge collection efficiency (Figure S3, Supporting Information). Moreover, our optimized perovskite diodes possessed power conversion efficiencies >12% working in a photovoltaic mode (Figure S4, Supporting Information), which confirms the quality of the junction morphology and efficient charge collection.

Having established that the optimized Type 4 structure delivered very low dark currents and high, broad visible-band EQEs, we carefully evaluated the key photodiode performance metrics: LDR; detectivity; noise figure of merit; and temporal (frequency) response. The LDR is particularly important for

DOI: 10.1002/adma.201405171

image sensors since they need to operate over a broad intensity range. To evaluate the LDR, we chose the best Type 4 device, and performed intensity-dependent photocurrent measurements. The LDR is commonly expressed in a logarithmic scale as

$$\mathrm{LDR} = 20\log\frac{J_{\mathrm{upper}}}{J_{\mathrm{lower}}} = 20\log\frac{L_{\mathrm{upper}}}{L_{\mathrm{lower}}} \quad (1)$$

where, J and L denote the current density and input light irradiance, respectively. The upper limit of the LDR is given by the current value that deviates from linearity, and is defined by the slower carrier transit time.[27] Although the charge carrier mobility of perovskites is yet to be reliably measured, estimates of electron and hole mobilities of the order 20 $cm^2\ V\ s^{-1}$[11] have been reported. This is at least four orders of magnitude larger than the electron mobility of fullerenes.[28] Therefore, the upper limit of the linearity range will be defined by the space charge limited current in the fullerene layer, and as such

$$J_{\mathrm{upper}} = \frac{C_{\mathrm{f}}(V_{\mathrm{bi}} + V_{\mathrm{RB}})}{t_{\mathrm{tr}}} \approx \frac{\varepsilon_{\mathrm{f}}\varepsilon_0\mu_{\mathrm{f}}V^2}{d_{\mathrm{f}}^3} \quad (2)$$

where C_{f} is the capacitance per unit area of the fullerene layer, t_{tr} the transit time of the electrons in the fullerene layer, ε_{f} the fullerene dielectric constant, ε_0 vacuum permittivity, μ_{f} fullerene electron mobility ($\approx 3\times10^{-3}$ $cm^2\ V\ s^{-1}$),[27] V_{bi} and V_{RB} the built-in and reverse bias voltages, and d_{f} the combined fullerene layer thickness (≈180 nm). Equation (2) predicts an upper limit of ≈0.2 A cm^{-2}. This is close to our experimental observations, as shown in **Figure 2**a (intensity dependence at –0.5 V) supporting this analysis. The Type 4 photodiode has a linear response from 1.8 nW cm^{-2} to 0.4 W cm^{-2} corresponding to a LDR of ≈170 dB (at –0.5 V). The lower limit of the LDR is governed by the detection limit of our equipment. To gain a more accurate view of the actual LDR, we also measured the noise spectral power (Figure S5, Supporting Information). At reverse bias voltages between 0 and –1 V the noise current was found to be ≈50 fA $Hz^{-1/2}$ corresponding to a noise equivalent power (NEP) of ≈200 fW $Hz^{-1/2}$ with device area 0.2 cm^2. The predicted and theoretical LDR values can be estimated based upon this NEP to be 230 and 250 dB, respectively. The shot noise current can also be calculated from the dark current to be 7 fA $Hz^{-1/2}$ (at –0.5 V), that is, these are very low noise photodiode.

The specific detectivity was determined based upon the measured EQE and noise current as described in ref.[14]. These results are provided in Figure 2b for the optimized Type 4 device under several reverse bias voltages. We note detectivities $>10^{12}$ J across the UV–visible, very close to those in silicon photodiodes[2,3] with a completely IR-blind response. Finally, we measured the frequency response of the optimized Type 4 device and this is shown in **Figure 3**a: normalized photocurrent versus light modulation frequency at different bias voltages (see Experimental Section for details). In Figure 3a, a typical frequency-dependent response of a Type 1 device (thin PC60BM) is also shown to highlight the important role of the thick PC60BM/C60 interlayer that is used in the Type 4 device. Figure 3b presents the –3 dB point frequency ($f_{-3\mathrm{dB}}$) for both Type 1 and 4 devices, which we find to be ≈150 and 500 kHz, respectively.

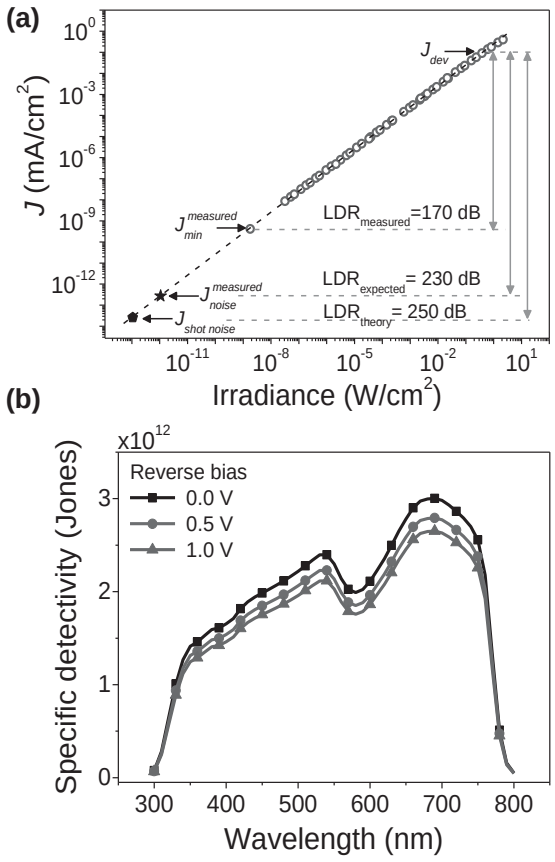

Figure 2. Optimized Type 4 photodiode performance metrics. a) Photocurrent versus irradiance measured at –0.5 V and illumination wavelength of 532 nm: the linear response extends over 170 dB. The lower limit of the linearity is governed by the measurement limit. The measured noise current density and calculated shot noise current density are marked and correspond to a LDR of 230 and 250 dB, respectively. b) Specific detectivity at three reverse bias voltages.

The superior frequency response of the Type 4 device is due to its reduced parasitic capacitance that decreases the overall RC constant of the circuit (see the equivalent circuits inset in Figure 3b and also the capacitance measurements in Figure S6, Supporting Information). In this regard, the $f_{-3\mathrm{dB}}$ values are in agreement with those calculated from Equation (3) valid for $R \gg t_{\mathrm{tr}}$, which is the case here for our relatively large 0.2 cm^2 devices

$$f_{-3\mathrm{dB}} = \frac{1}{2\pi RC} \quad (3)$$

We note that the frequency response of the Type 4 device is more than adequate for image sensing and comparable with, or superior to, many commercial inorganic photodiodes operating in the visible band with similar active area as our devices.[29] In the small-pixel limit with negligible parasitic capacitance, the $f_{-3\mathrm{dB}}$ response will be limited by the electron transit time in the fullerene layer. According to Equation (4) this would mean, for example, a 6 MHz response at –0.5 V

$$f_{3\mathrm{dB}} = \frac{3.5}{2\pi t_{\mathrm{tr}}} = \frac{3.5\mu_{\mathrm{f}}(V_{\mathrm{bi}} + V_{\mathrm{RB}})}{2\pi d_{\mathrm{f}}^2} \quad (4)$$

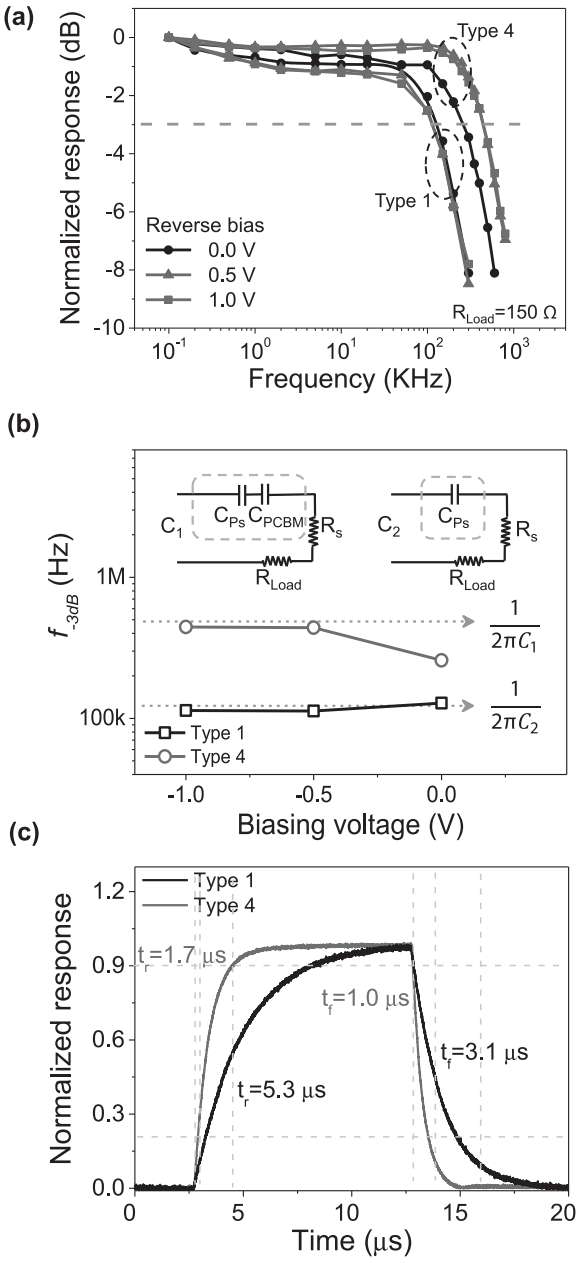

Figure 3. Temporal response of Type 1 and Type 4 devices. a) Normalized photocurrent versus incident light modulation frequency (irradiance = 50 mW cm^{-2}; 470 nm as representative of the LDR and EQE responses). The Type 4 devices exhibit a higher f_{-3dB} compared to Type 1. b) Measured f_{-3dB} versus bias voltage. Inset shows the equivalent circuit and the dotted lines the expected f_{-3dB} values based upon the total circuit *RC* (Load resistance = 150 Ω). c) Temporal response (–0.5 V bias) with standard 90%-response rise and fall times shown.

The predicted value of 6 MHz is close to the value recently reported by Dou et al.,[30] that is, 3 MHz for very small area photodiodes (0.01 cm^2).

To further demonstrate the temporal response of these photodiodes, Figure 3c shows the current transients for Type 1 and 4 devices at –0.5 V from which the rise and fall times can be determined (of order 1 µs for the Type 4 device). The transient signals for the Type 4 devices are clean and flat, typical of what one would observe in a conventional silicon photodiode with no initial rise in the on-state often seen in organic and quantum dot photodiodes due to charge trapping/detrapping.[31]

In summary, we have demonstrated an organohalide perovskite low noise, IR-blind visible photodiode with performance metrics equivalent to commercial inorganic semiconductor devices. The perovskite photodiode consists of a simple, solution-processed homojunction capped with a PC60BM/C60 cathode interlayer. This interlayer: i) behaves as a low shunt capacitor improving the diode temporal response; ii) suppresses the dark current by conformally coating the perovskite homojunction and limiting the back injection of holes; and iii) provides electro-optical control of the spectral response. These features are achieved without compromising the LDR as the fullerene electron mobility is sufficient to prevent space charge forming in the junction up to light intensities of 0.4 W cm^{-2}. We observe a measurement-limited LDR of ≈170 dB (at –0.5 V), but noise calculations would indicate it could be as high as 250 dB. This work further demonstrates the remarkable potential of the organohalide perovskites in optoelectronics, and provides a technology relevant silicon substitute for visible light detection and imaging.

Experimental Section

Materials: Lead iodide (PbI_2, beads, 99.999% trace metals basis) was purchased from Sigma Aldrich and methylammonium iodide (MAI, MS101000-10) was purchased from Dyesol Pty Ltd. PEDOT:PSS was obtained from Heraeus (Clevios P VP. Al 4083, Charge: 2014P0168). PC60BM and C60 were purchased from ADS. All commercial products were used as received.

Device Fabrication: All PPDs were fabricated on commercial ITO patterned glass electrodes (15 Ω sq^{-1}: Kintec) in a class 1000 clean room. The ITO electrodes were cleaned in a detergent solution (Alconox) bath at 70 °C for 10 min, followed by sonication in sequence with Alconox, Milli-Q water, acetone, and 2-propanol for 10 min each. The cleaned substrates were dried with nitrogen before being coated with 30±5 nm PEDOT:PSS by spin-coating at 5000 rpm for 30 s. The PEDOT:PSS coated substrates were heated on a hot plate at 170 °C for 10 min. After cooling, the substrates were transferred into a nitrogen-filled glove box for device fabrication (O_2 < 1 ppm, H_2O < 1 ppm). $CH_3NH_3PbI_3$ perovskite thin films were spin-coated as per the method reported by Jeon et al.[20] Typically, 461 mg PbI_2 and 159 mg MAI were dissolved in 1 mL of a mixed solvent of γ-butyrolactone (GBL) and dimethyl sulfoxide (DMSO) (7:3 v/v) with stirring and heating at 60 °C for 2 h. 200 µL of the $CH_3NH_3PbI_3$ solution was dispensed onto the PEDOT:PSS layer and spin-coated at 1000 rpm for 10 s. The spin speed was then increased to 5000 rpm, and after 30 s, 200 µL of toluene was dispensed onto the middle of the spinning "wet" perovskite film in less than 2 s. Finally, the films were left to spin at 5000 rpm for 20 s. The spin-coating was done at room temperature (20–25 °C). After depositing the perovskite layer, a 10 mg mL^{-1} PC60BM in toluene solution was spin-coated onto the $CH_3NH_3PbI_3$ perovskite layer at a spin speed of 1000 rpm for 40 s to form a thin PC60BM layer (Type 1 devices), or a 25 mg mL^{-1} PC60BM in toluene solution was spin-coated onto the $CH_3NH_3PbI_3$ perovskite layer at a spin speed of 800 rpm for 40 s to form a thick PC60BM layer (Type 2). The devices were heated on a hot plate at 70 °C for 10 min. For comparison, 130 nm of C60 was evaporated at 400 °C, under a 10^{-5} mbar vacuum at a deposition rate of 0.6 Å s^{-1} onto a $CH_3NH_3PbI_3$ perovskite layer (Type 3) or a thick PC60BM layer (Type 4), respectively. Finally, 1 nm of LiF and 100 nm of Ag were deposited by thermal evaporation under a 10^{-6} mbar vacuum with an appropriate mask (0.2 cm^2 for each device) to complete the device. All devices were encapsulated for device performance measurements. A standard encapsulation protocol was used, namely: epoxy resin (XNR 5516Z-B1,

Adv. Mater. 2015,
DOI: 10.1002/adma.201405171

Nagase ChemteX Corporation) was screened onto the edges of a capping glass plate, which was then placed onto the photodiodes firmly before being illuminated under UV light for 10 min.

Characterization: Optical absorption spectra were collected using a Cary 5000 UV–vis spectrophotometer. The crystallinity of the films was characterized by XRD. All XRD spectra were obtained on a Bruker Advance D8 X-ray diffractometer equipped with a LynxEye detector, Cu tube (CuKα = 1.5418 A) and operated at 40 kV with a 2θ scan range of 10°–70°. The surface morphology of the perovskite films were imaged using a Hitachi SU3500 SEM with an accelerating voltage of 10 keV. Film thicknesses were determined using a surface profilometer (Veeco Dektak 150). The capacitance of the devices was measured by the charge extraction by linearly increasing voltage (CELIV) technique as explained in detail in ref. [27].

Device Performance Measurements: The current density–voltage (*J*–*V*) characteristics were recorded using an Agilent B1500A Semiconductor Analyzer in the dark with a scan speed of 0.01 V s^{-1}. EQE spectra and the near normal incidence reflectance of the devices were recorded with a PV Measurements Inc. QEX7 system, which was calibrated with a NREL certified photodiode without light bias. Frequency response measurements were obtained using an NSPB500AS Nichia blue LED modulated using an Agilent 33250A arbitrary wave function generator. The photocurrent responses of the photodiodes were recorded using a digital storage oscilloscope (LeCroy Waverunner A6200). LDRs were determined using a second harmonic Nd:YAG laser (Laserver) operating continuously at 532 nm as the illumination source with a series of neutral density filters purchased from Thorlabs and Holmarc used to vary the light intensity. The light intensity was calibrated by a standard photodiode simultaneously to compensate for intensity fluctuations and the current response was recorded by an Agilent B1500A Semiconductor Analyzer.

Note: During the review process of this manuscript, a related paper discussing the $CH_3NH_3PbI_3$ perovskite photodiodes was published.[30]

Supporting Information

Supporting Information is available from the Wiley Online Library or from the author.

Acknowledgements

Q.L. and A.A. contributed equally to this work. PLB is a UQ Vice Chancellor's Senior Research Fellow and PM is an ARC Discovery Outstanding Researcher Award Fellow. Q.L. is supported by an International Postgraduate Research Scholarship (IPRS). This work was performed in part at the Queensland node of the Australian National Fabrication Facility (ANFF): a company established under the National Collaborative Research Infrastructure Strategy to provide nano and micro fabrication facilities for Australia's researchers. The authors acknowledge the facilities, the scientific and technical assistance of the Australian Microscopy & Microanalysis Research Facility at the Centre for Microscopy and Microanalysis, The University of Queensland. This Program has also been supported by the Australian Government through the Australian Renewable Energy Agency (ARENA) Australian Centre for Advanced Photovoltaics. Responsibility for the views, information or advice expressed herein is not accepted by the Australian Government.

Received: November 12, 2014
Revised: December 14, 2014
Published online:

[1] V. Sukhovatkin, S. Hinds, L. Brzozowski, E. H. Sargent, *Science* **2009**, *324*, 1542.
[2] X. Gong, M. Tong, Y. Xia, W. Cai, J. S. Moon, Y. Cao, G. Yu, C.-L. Shieh, B. Nilsson, A. J. Heeger, *Science* **2009**, *325*, 1665.
[3] G. Konstantatos, J. Clifford, L. Levina, E. H. Sargent, *Nat. Photonics* **2007**, *1*, 531.
[4] F. Guo, B. Yang, Y. Yuan, Z. Xiao, Q. Dong, Y. Bi, J. Huang, *Nat. Nanotechnol.* **2012**, *7*, 798.
[5] T. Rauch, M. Boberl, S. F. Tedde, J. Furst, M. V. Kovalenko, G. Hesser, U. Lemmer, W. Heiss, O. Hayden, *Nat. Photonics* **2009**, *3*, 332.
[6] A. Armin, M. Hambsch, I. K. Kim, P. L. Burn, P. Meredith, E. B. Namdas, *Laser Photonics Rev.* **2014**, *8*, 924.
[7] M. M. Lee, J. Teuscher, T. Miyasaka, T. N. Murakami, H. J. Snaith, *Science* **2012**, *338*, 643.
[8] J. Burschka, N. Pellet, S.-J. Moon, R. Humphry-Baker, P. Gao, M. K. Nazeeruddin, M. Grätzel, *Nature (London)* **2013**, *499*, 316.
[9] Q. Lin, A. Armin, R. C. R. Nagiri, P. L. Burn, P. Meredith, *Nat. Photonics* DOI: 10.1038/NPHOTON.2014.284.
[10] J. M. Frost, K. T. Butler, F. Brivio, C. H. Hendon, M. van Schilfgaarde, A. Walsh, *Nano Lett.* **2014**, *14*, 2584.
[11] T. Leijtens, S. D. Stranks, G. E. Eperon, R. Lindblad, E. M. Johansson, I. J. McPherson, H. Rensmo, J. M. Ball, M. M. Lee, H. J. Snaith, *ACS Nano* **2014**, *8*, 7147.
[12] G. Xing, N. Mathews, S. S. Lim, N. Yantara, X. Liu, D. Sabba, M. Grätzel, S. Mhaisalkar, T. C. Sum, *Nat. Mater.* **2014**, *13*, 476.
[13] K. G. Lim, H. B. Kim, J. Jeong, H. Kim, J. Y. Kim, T. W. Lee, *Adv. Mater.* **2014**, *26*, 6461.
[14] M. Liu, M. B. Johnston, H. J. Snaith, *Nature (London)* **2013**, *501*, 395.
[15] D. M. Lyons, A. Armin, M. Stolterfoht, R. C. R. Nagiri, R. D. J.-V. Vuuren, B. N. Pal, P. L. Burn, S.-C. Lo, P. Meredith, *Org. Electron.* **2014**, *15*, 2003.
[16] A. Mei, X. Li, L. Liu, Z. Ku, T. Liu, Y. Rong, M. Xu, M. Hu, J. Chen, Y. Yang, *Science* **2014**, *345*, 295.
[17] J. H. Heo, S. H. Im, J. H. Noh, T. N. Mandal, C.-S. Lim, J. A. Chang, Y. H. Lee, H.-J. Kim, A. Sarkar, M. K. Nazeeruddin, *Nat. Photonics* **2013**, *7*, 486.
[18] D. Liu, T. L. Kelly, *Nat. Photonics* **2013**, *8*, 133.
[19] E. J. Juarez-Perez, R. S. Sanchez, L. Badia, G. Garcia-Belmonte, Y. S. Kang, I. Mora-Sero, J. Bisquert, *J. Phys. Chem. Lett.* **2014**, *5*, 2390.
[20] N. J. Jeon, J. H. Noh, Y. C. Kim, W. S. Yang, S. Ryu, S. I. Seok, *Nat. Mater.* **2014**, *13*, 897.
[21] H.-R. Xia, J. Li, W.-T. Sun, L.-M. Peng, *Chem. Commun.* **2014**, *50*, 13695.
[22] X. Hu, X. Zhang, L. Liang, J. Bao, S. Li, W. Yang, Y. Xie, *Adv. Funct. Mater.* **2014**, *24*, 7373.
[23] Y. Lee, J. Kwon, E. Hwang, C. H. Ra, W. J. Yoo, J. H. Ahn, J. H. Park, J. H. Cho, *Adv. Mater.* **2015**, *27*, 41.
[24] G. F. Burkhard, E. T. Hoke, M. D. McGehee, *Adv. Mater.* **2010**, *22*, 3293.
[25] A. Armin, M. Velusamy, P. Wolfer, Y. Zhang, P. L. Burn, P. Meredith, A. Pivrikas, *ACS Photonics* **2014**, *1*, 173.
[26] L. A. Pettersson, L. S. Roman, O. Ingänas, *J. Appl. Phys.* **1999**, *86*, 487.
[27] A. Armin, G. Juška, B. W. Philippa, P. L. Burn, P. Meredith, R. D. White, A. Pivrikas, *Adv. Energy Mater.* **2013**, *3*, 321.
[28] A. Armin, G. Juška, M. Ullah, M. Velusamy, P. L. Burn, P. Meredith, A. Pivrikas, *Adv. Energy Mater.* **2014**, *4*, 1300954.
[29] http://www.hamamatsu.com/resources/pdf/ssd/s1087_etc_kspd1039e.pdf and http://www.hamamatsu.com/resources/pdf/ssd/g1115_etc_kgpd1002e.pdf, (accessed January 2015).
[30] L. Dou, Y. M. Yang, J. You, Z. Hong, W.-H. Chang, G. Li, Y. Yang, *Nat. Commun.* DOI:10.1038/ncomms6404.
[31] C. R. McNeill, I. Hwang, N. C. Greenham, *J. Appl. Phys.* **2009**, *106*, 024507.